Volume 18, Number 5, 2025. pp. 705-724

Jordan Journal of Physics

ARTICLE

Proton Transmission through Magnetic Lenses for Characterizing Water and Human Tissues via Proton Radiography

Fatemeh Namdari and **Seyede Nasrin Hosseinimotlagh**

Department of Physics, Shiraz Branch, Islamic Azad University, Shiraz, Iran.

Doi: **https://doi.org/10.47011/18.5.11**

Received on: 29/01/2025; *Accepted on: 07/04/2025*

Abstract: Proton radiography (PR) is a new imaging method that allows direct measurement of the proton energy dissipation in different tissues. Proton radiography enables fast and effective high-precision lateral alignment of the proton beam and target volume in human irradiation experiments with limited dose exposure. The benefits of PR can be summarized as: 1) high image resolution, 2) the complete field of view can be measured with one short proton spill, 3) short data acquisition time, and 4) simple data processing. Enhancing image contrast can be achieved by substituting cuts on the scattering angle with the use of a magnetic lens (ML) system, resulting in optimal images of objects. The current study is primarily focusing on proton acceleration via target normal sheath acceleration (TNSA) using nanowire-coated foils as targets, followed by an investigation of the LET, range, and dose of protons. In this work, simplified physical models of proton transport, including Bethe–Bloch energy loss, energy straggling, and multiple Coulomb scattering (MCS), are used in the 0–300 MeV energy range of interest to analytically quantify the tradeoffs and scaling relationships between dose, spatial resolution, density resolution, and voxel size. We found that dose (D) is directly influenced by the size of voxel α and the necessary density resolution δ, which highlights a very strong dependence on voxel size. Our work shows that the average dose increases with increasing number of protons, while the average dose decreases with increasing proton beam energy, which is in good agreement with the other references. These studies demonstrate that the dose D of water, breast, brain, lung, and eye tissues is directly influenced by the size of voxel α and the necessary density resolution δ, adhering to the relationship $D \propto \alpha^{-5}\delta^{-2}$, which highlights a very strong dependence on voxel size.

Keywords: Magnetic lenses, PR, Tissue characterization, Radiation dose, Image blurring, Diagnostic imaging.

1. Introduction

A new diagnostic technique, high-energy proton radiography (PR), is being used to investigate the imaging of objects [1-3]. The three key events affecting protons as they pass via a material are absorption, energy dissipation, and multiple Coulomb scattering (MCS). PR has not been utilized for a prolonged time due to the MCS causing image blurring in radiography. A crucial method used in PR development involves a magnetic imaging lens system situated between the image and object, which focuses the proton beam (PB) point-to-point and achieves the resolution required across the full field of view for radiography [3–10].

More recently, it has been shown that many of the advantages of protons as a radiographic probe can be realized by using a magnetic lens to focus on the transmitted proton beam. Some potential advantages of protons over conventional X-ray techniques for flash radiography of thick, dense, dynamic systems include: 1) high penetrating power, 2) high detection efficiency, 3) small scattered background, 4) no need for a conversion target and the consequent phase-space broadening of the beam, 5) inherent multi-pulse capability, and 6) large stand-off distances from the test object and containment vessel to the detectors. Additionally, the use of a magnetic lens with thin

Corresponding Author: Seyede Nasrin Hosseinimotlagh **Email**: hosseinimotlagh@iaushiraz.ac.ir

detectors allows multiple images on a single axis, though progressively smaller apertures to be used to vary the magnitude and Z-dependence of the interaction, and can provide material identification. In addition, mono-energetic protons offer advantages over X-rays in the visualization of internal bodily structures. Thus, unlike X-rays and neutrons whose flux is exponentially attenuated with respect to absorber thickness, proton flux is only moderately attenuated before falling off steeply at the end of the particle range. This property may be used to advantage by placing a photographic film in the region of very steep attenuation, when radiographs of very high contrast may be obtained. A further advantage is that radiography based on proton transmission is relatively insensitive to variations in the chemical composition of the tissues [10-16]. This work utilizes a radiography technique that employs protons with high energy as probe particles. The effectiveness of this method relies on the use of magnetic lenses (MLs) to counteract the small MCS angle caused by the passage of charged protons through the object under investigation. Employing an ML renders the side effects of MCS perturbation a valuable and fulfilling endeavor. Protons exhibit distinct dependencies on material properties, influenced by a combination of Coulomb scattering at small angles, nuclear scattering, and energy dissipation processes, each with unique characteristics related to electron configuration, atomic number, density, and atomic weight. These tips enable the simultaneous estimation of the amount of matter and its identity [17-25].

However, protons suffer a significant amount of elastic scattering with nuclei through their trajectory in the form of multiple Coulomb scattering (MCS), which severely reduces the spatial resolution of proton imaging. Advanced trajectory estimation methods have successfully helped address the problem of MCS in proton imaging, ameliorating the spatial resolution. In PR, the images are blurred because of MCS. Thus, it is important to find the best way to reduce the impact of MCS on the extracted proton energy loss radiographic image to minimize the blurring and, consequently, to improve the accuracy of the energy-loss map. To suppress this kind of blurring, a magnetic structure called the Zumbro lens was developed by Mottershead and Zumbro [1], which is now the most important part of the PR system. The Zumbro lens is designed according to the momentum of the transmitted proton [8, 9]. As a result, the lens provides point-to-point focusing from the object to the image without blurring for protons whose momentum matches the reference value. The basic configuration of the PR system consists of three key parts: the diffuser, the matching lens, and a Zumbro lens. In the system, the proton beam propagates from left to right. A pencil monoenergetic proton beam is first scattered by a diffuser. After acquiring a broader angular distribution, it is transported into the matching lens. Both the angle and size of the beam are modified in the matching lens according to the coordinate-angle correlation required by the Zumbro lens. Then, the protons with this correlation can be imaged by the Zumbro lens upon reaching the image plane.

The multiphase interaction allows adjustments to be made to the sensitivity of the technique, thereby enhancing its utility across various material thicknesses. The magnetic optic enables unit magnification between the image and object and allows the detector planes and image to be moved away from the object being tested [26-27]. This significantly enhances the signal-to-background ratio. The ML system allows for adjustable angular acceptance, which is essential for material identification and enables the system to be sensitive to objects of varying thicknesses. Protons offer additional advantages as probe particles in radiography due to their high detection yield and the ability to be recorded repeatedly using a multilayer detector. In applications where dense objects require multiple rapid radiographs, consecutive velocities, protons are nearly an ideal solution due to their high penetration capabilities. This is because devices that accelerate protons produce long trains of high-intensity and short-duration beams, which are needed for these applications. Furthermore, advancements in technology have made available high-resolution, high-velocity proton data recordings, allowing for accurate results in energetic experiments, as well as in proton computed tomography (PCT). The range, as well as the transverse displacements and their angles, of the input protons can now be measured, for instance, by employing calorimeters and detectors.

This approach bears a strong resemblance to XRCT methods [1-8, 28-30]. 1) The average energy dissipation method involves gathering

statistics for a set of paths, with a focus on quantitatively assessing the average energy dissipation per path. Proton radiographs taken from multiple viewpoints can then be used to perform PCT in the same manner as X-ray computed tomography (XRCT) or PET, even when the paths of the protons are not completely straight. Many imaging methods can predictably quantify the dose-resolution relationship, as well as spatial and density resolution, in an ideal diagnostic system scenario. Two specific methods were chosen. Statistics for every category of proton path, not limited to a straight line, are compiled from within the imaged object. The proportion of protons transferred to each respective pathway is known as the "transfer efficiency" quantity. This method and XRCT are similar to each other. [1-8, 28-30]. 2) The mean energy dissipation method collects a set of statistical paths, but is qualitatively interested in determining the mean energy dissipation on every path. In fact, it turns out that the use of protons instead of X-rays for transmission imaging has some disadvantages. These include the need for large, expensive equipment to produce proton beams (e.g., a cyclotron or synchrotron) and the limitations on image quality arising from the multiple scattering of protons. However, the advantages of PR include a lower patient dose, higher soft-tissue contrast than X-rays, and real-time capability for tumor tracking within tissue [11–13]. PR also offers an improved contrast-to-noise ratio compared with standard X-ray imaging.

Verification of patient-specific proton stopping powers obtained in the patient's treatment position can be used to reduce the distal and proximal margins needed in particle beam planning. Proton radiography can be used as a pre-treatment instrument to verify integrated stopping power consistency with the treatment planning CT. Although a proton radiograph is a pixel-by-pixel representation of integrated stopping powers, the image may also be of high enough quality and contrast to be used for patient alignment. This investigation quantifies the accuracy and image quality of a prototype proton radiography system on a clinical proton delivery system. The highest level of spatial resolution can be attained by employing the most advanced methods to reconstruct the individual path, which is primarily constrained by the physical properties of the MCS phenomenon. This paper investigates ways to attain high image quality with high contrast in PR employing MLs in PCT. The structure of the paper is as follows. Section 2 presents a laser-driven proton accelerator based on target normal sheath acceleration (TNSA) using nanowire-coated foils as targets. Section 3 discusses the interaction of protons with matter. Section 4 examines proton imaging quality. Section 5 compares high-energy PR with other imaging techniques. Section 6 presents a theoretical investigation of PR along with numerical results. Finally, the discussion and conclusions are provided.

2. Laser-Driven Proton Accelerator

The higher flux and temperature of hot electrons that propagate into the target enable the use of nanostructured targets to accelerate protons or light ions via target normal sheath acceleration (TNSA) when a foil a few μm thick is used as the substrate for the nanostructures. According to the TNSA scheme (Fig.1), relativistic electrons produced during the interaction between an ultra-intense laser pulse and a thin foil cross the target and escape from its rear surface, generating a sheath electric field of several TV/m. Therefore, nearby ions, including protons adsorbed on the target surface as impurities, accelerated in the forward direction at energies of up to several tens of MeV per nucleon [31-33]. The capability of nanostructured targets to improve laser-target coupling and electron acceleration suggests the possibility of producing compact electron or proton beam sources using optimized structured targets and controlled irradiation conditions.
Since different target geometries are suitable for different scopes, it is important to achieve a deeper understanding of the interaction mechanisms and processes involved in this system in order to optimize the experimental conditions for various applications. Experimental and numerical studies suggest, for example, that the size of the gaps between nanostructures, such as the spacing between nanowires or the channel size in a nanotube, plays a key role in the interaction. Larger gaps seem in fact to favor the acceleration of high-energy electrons via plasmonic effects, whereas small gaps give rise to a stochastic heating that produces a hot, dense plasma [34-39].

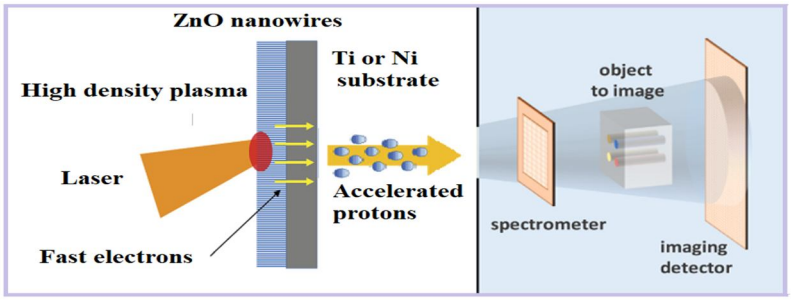

FIG. 1. Scheme showing proton acceleration via target normal sheath acceleration (TNSA) using nanowire-coated foils as targets with illustration of laser-driven PR.

3. Interaction of Protons with Matter

In PR, several interaction processes with matter have to be considered. These mainly include energy loss, nuclear interactions, and multiple Coulomb scattering.

3.1. Energy Loss

The energy loss of charged particles in matter is described by the Bethe-Bloch formula: $-dE/dx = \frac{4\pi k_0^2 z^2 e^4 n_e}{m_e c^2 \beta^2 \rho}[ln\frac{2m_e c^2\beta^2}{I(1-\beta^2)} - \beta^2 - \frac{\delta(\beta)}{2} - \frac{C(\beta)}{2}]$, where $k_0 = 8.99 \times 10^9 Nm^2C^{-2}$, z = atomic number of the projectile, e = electron charge, n_e = electron density of the medium, m_e = electron mass, c = speed of light, $\beta = v/c$ = relativistic beta factor, ρ = density of the medium, I = mean excitation energy in eV. It is dependent on the thickness, density, and composition of the target. The interaction in the target with the electrons of the target atoms leads to a non-uniform energy distribution of the exiting beam. This affects the point-to-point focusing as the Lorentz force, responsible for the bending of the particle trajectories, which is dependent on the particle velocity or beam direction, which is directly correlated to the particle energy. This causes dispersion in the magnets, leading to a z-shift of the focal spot x_i in the image plane. It is difficult to estimate the quantitative effect of the energy loss on the spatial resolution performance of a radiographic setup, mainly because of the unknown influence of the used collimator. Assuming that particles experiencing more energy loss also exit the target with a larger scattering angle due to more interactions, these particles will be the ones traveling further away from the beam axis at the location of the Fourier plane. The mid-plane collimator will sort out the particles; therefore, this effect can partly be canceled by choosing a different collimator.

3.2. Nuclear Interactions

In case of nuclear interactions, we have to differentiate between elastic nuclear collisions and inelastic nuclear interactions. The elastic collisions cause large scattering angles and possibly even a recoil of the proton. In this case, the interaction between the incident protons and the nuclei of the target happens through charge, as described in the following section on MCS. If the velocity of the incident proton is large enough to overcome the electrostatic potential of the nucleus, a nuclear reaction will happen. In this reaction, which is considered an inelastic interaction, the protons are first absorbed by the target nuclei, forming a new compound nucleus. These nuclei are mostly unstable and break up into various fragments, being ejected from the initial nucleus. The process is also called spallation and happens through strong interaction; it is dominant for the high energies used for PR. Although both types of interaction usually lead to a removal of the involved primary proton from the particle distribution, the total cross-section for the processes, and therefore the effect on the total particle distribution at the image plane of a radiographic setup, is very small. By integrating the differential cross-section for nuclear collisions outside of the angular acceptance of the utilized radiographic setup, the removal probability can be determined; however, this quantity is not measured continuously at the high energies required for PR. Therefore, a simple approximation can be introduced. For sufficiently high beam energies above 1 GeV, the probability for a scattering event is related to the nuclear collision length λ_{nc} [38]. Using the exponential attenuation law known as the Lambert-Beer law, the transmission can then be described by: $T_{nucl} = e^{-x/\lambda_{nc}}$. The corresponding nuclear collision lengths are tabulated by the particle data group [39]. Due to

the small cross-section, the influence of nuclear collisions on the total transmission is naturally very small, but will increase for thick or dense targets.

4. Image Quality

The image quality of a radiographic setup depends mainly on three factors: chromatic aberrations, scattering, and detector blur.

4.1. Chromatic Aberrations

Chromatic aberrations lead to the definition of the chromatic length. This effect is dependent on the properties and geometry of the object of interest, which directly affect the scattering φ and the energy loss straggling δ. This may lead to an effect known as limning, which particularly affects regions with steep density transitions.

4.2. Scattering

Scattering in the object, especially MCS, results in a non-zero scattering angle of the exiting proton but may also cause a shift of the trajectory. It is proportional to the square root of the target thickness and is also $\propto 1/p$, where p is the proton momentum.

4.3. Detector Blur

Protons interacting in the used scintillation generally do not travel on a trajectory parallel to the beam axis but rather traverse the material with an angle determined by the focusing properties of the lens system. This leads to a non-parallel emission of photons by a single proton track, an effect that can be partially reduced by selecting scintillators grown from columnar crystals capable of containing the produced photons in one column by total reflection. The effect can also be decreased by using thin scintillators, which in turn decreases the total yield of light [38-39]. Detector blur is also boosted by secondary particles, which are created during scattering processes of primary protons in the scintillation material. Summarizing the above findings, the detector blur is $\propto 1/p$ and decreases with increasing proton energy. All of the effects above tend to scale inversely with the proton energy, suggesting that an increase in the particle energy would lead to infinitely good spatial resolution performance. However, this is not the case for several reasons. Choosing higher proton energies will decrease the amount of scattering and therefore require longer collimators with smaller angular acceptances, which are not only complicated to handle in terms of alignment but also deliver worse results. This is obvious as the collimator has to be long or dense enough to at least deflect unwanted parts of the angular proton distribution so that those protons do not contribute to the final image.

5. High-Energy PR vs. Other Techniques

Currently, the most prominent candidates for future medical imaging alongside high-energy PR are single-tracking pCT and DECT. DECT is already clinically available and has been shown to deliver good results for treatment planning; however, its material separation capability is mainly used to improve image quality. This includes reducing artifacts originating from parasitic high-Z materials or enabling the visualization of contrast agents, for example, for the analysis of renal function or renal stones. Compared with conventional XCT, DECT neither offers increased data acquisition speed nor improves the spatial resolution performance of the system. In contrast, tracking pCT offers, compared with current high-energy PR, the possibility of simultaneously measuring both the density of the sample via scattering and the stopping power by employing a range telescope. As the requirements on the accelerator side are relatively low, a large number of research groups worldwide are addressing the challenges of this technique. Despite significant advancements in recent years, the major limitations of this method remain the speed of data acquisition, particularly for scattering data), as well as constraints on the size of the object being investigated. Both factors are critical for clinical adoption, since maintaining a patient in a fixed position is more difficult in a constricting environment, which may also cause stress. In terms of dose deposition and image quality, tracking PCT is quite similar to conventional XCT. The requirements for novel PCT scanners, and more generally for any new clinical imaging technique, were discussed in the early 2000s [38] and remain valid today, as the parameters of conventional XCT, which serve as baseline values, have not changed significantly since then.

When comparing high-energy PR with tracking PCT, the advantages of PR clearly include outstanding spatial resolution in the

micrometer range, extremely short data acquisition times limited only by the capabilities of the accelerator, and generous space constraints that allow easy patient placement and handling due to the long range of high-energy protons in air. The crucial factors that still need to be addressed are dose deposition, which remains too high in the performed measurements, but may be reduced as suggested by the investigations conducted on proton flux dependent density measurements.

The tracking PCT performance may increase further during the next few years due to more computing power and better detector systems; however, the outlined problem of the narrow space available for patient positioning will remain. Summing up those findings, high-energy PR presents a promising alternative to current imaging techniques. Several improvements and upgrades will be required, but these may become available in the coming years. The unique capability of real-time online imaging during the treatment procedure, as well as the outstanding spatial resolution performance, could significantly boost the accuracy of current hadron therapy and make this technique very useful for clinics.

6. Theoretical Investigation of PR

6.1. Desired Particle Attenuation Length

By setting a constant regulation for incoming particles, one can estimate the optimal attenuation length λ in order to inspect particles during radiography of an object with a specified thickness L. The attenuation length λ is minimized when there is a relative error in estimating the number of particles transferred between two regions of the object under consideration, which vary in L and are distinct from T in terms of size. We begin with the fundamental assumption that the exponential decay of the beam through the object is: $N(L) = N_0 exp(-L/\lambda)$. We assume that N_0 is the number of incident particles per pixel. Therefore, the net number of particles passing through the two areas is as follows:

$$N(L) - N(L+T) = N_0 exp\left(-\frac{L}{\lambda}\right) - N_0 exp\left(-\frac{(L+T)}{\lambda}\right) = N_0 exp\left(-\frac{L}{\lambda}\right)\left[1 - \exp(-\frac{T}{\lambda})\right] \quad (1)$$

If $T \to 0$, then $\exp\left(-\frac{T}{\lambda}\right) \to 1 - \frac{T}{\lambda}$, and Eq. (1) converts to $N(L) - N(L+T) = N_0 exp\left(-\frac{L}{\lambda}\right)\left[\frac{T}{\lambda}\right]$ .Research findings indicate that the maximum absorption distance is equivalent to half the object thickness, with a specific ratio of λ = L/2.

6.2. MCS Mechanism

Coulomb scattering describes the deflection of charged particles in the electromagnetic potential of the nucleus of target atoms. During the passage, this process does not happen only once, but several times; therefore, it is also called MCS. In certain cases, MCS can affect the reconstruction of the initial scattering event and, consequently, degrade image quality. For thin objects, MCS is the dominant interaction process, as the cross-section for nuclear collisions is considerably smaller.

Unlike X-rays, when proton beams enter an object, they undergo multiple collisions with charged particles in the atoms of the object. As a result, they are scattered at small angles and propagate through the material. At first glance, MCS appears to be a significant drawback for PR because protons do not travel in straight lines over long distances, leading to image blurring caused by angular dispersion immediately after exiting the object. The angular distribution of protons emerging from the object due to MCS follows a Gaussian distribution, which can be characterized by its root mean square (rms) value. The initial deflection angle $\theta_0$in the plane of projection is defined by: $\theta_0(z) = 0.0136GeV(\beta cp)^{-1}\left(\frac{z}{X_0}\right)^{\frac{1}{2}}\left[1 + 0.038\ln(\frac{z}{X_0})\right]$ [11].

In this equation, c represents the light velocity, the proton velocity is βc, p is the proton linear momentum, and z parameter is the object's thickness, which is measured in the same unit as the length, denoted as X_0. It is important to note that the proton beta value is close to unity, and the angle θ_0 depends inversely on the proton momentum, while increasing significantly with $\sqrt{L}$, where L is the object thickness. We plotted a three-dimensional variation of $\theta_0(z)$ as a function of z and the energy of the incident proton (E), for water and various tissues including breast, eyes, brain, and lung in Fig. 2.

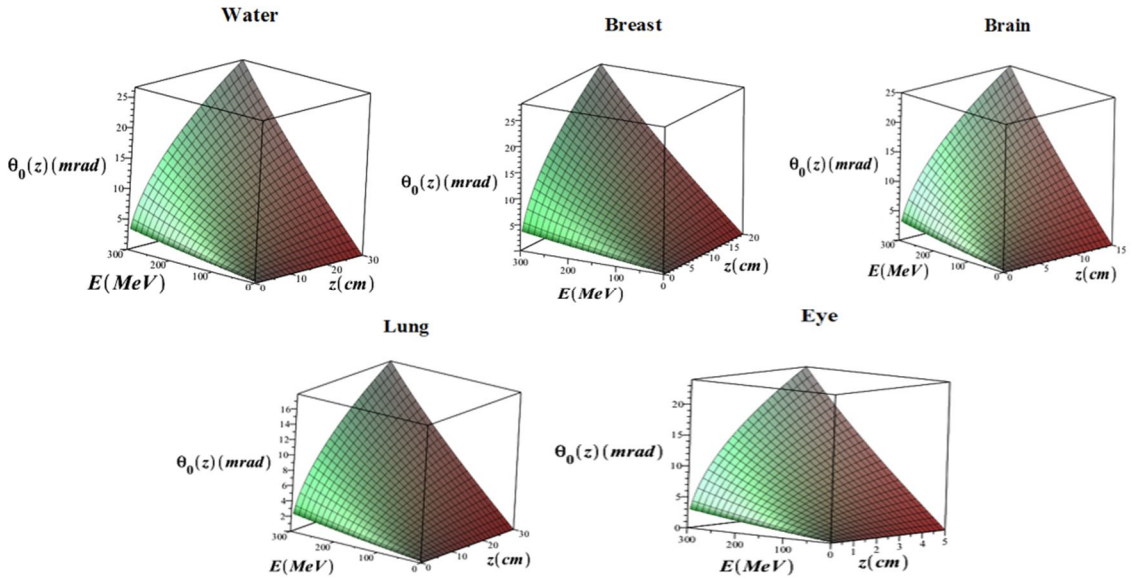

FIG. 2. 3-D diagram of $\theta_0(z)$ variations in terms of different values of z and E in water and in breast, eye, brain, and lung tissues.

MCS has two important effects on system performance. The first is a random effect that results in the limitation of object blurring, which is determined by the rms deviation of the image plane, y, upon the proton's arrival at the object's end from its non-scattered location. This deviation is expressed as: $y(z) = 3^{-1/2} z\theta_0(z)$. The 3-D diagram depicted in Fig. 3 illustrates variations of y (z) as a function of E and z in water and four distinct biological tissues, namely breast, eye, brain, and lung.

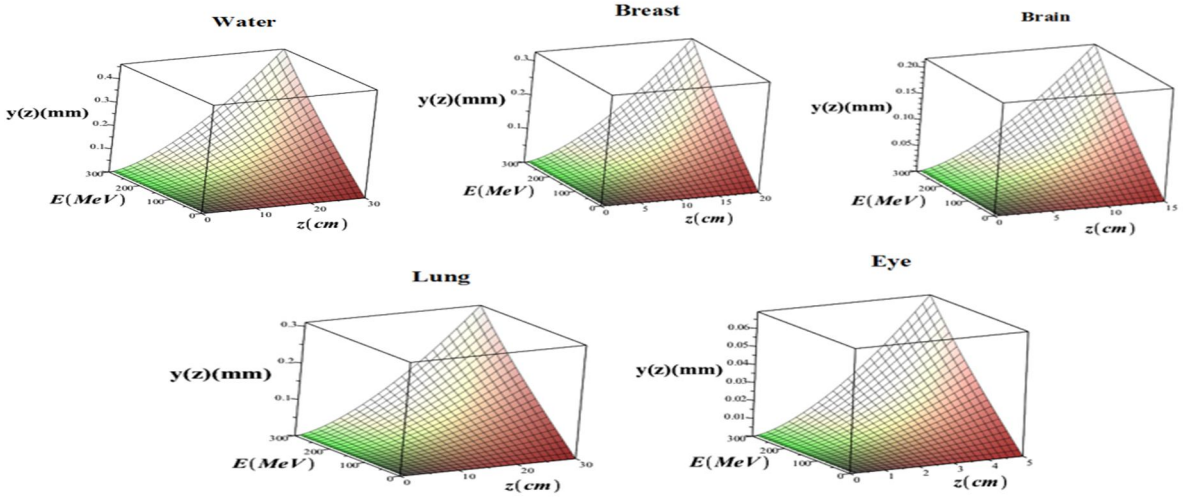

FIG. 3. The 3-D variations of $y\ (z)$ in terms of E and z in water and breast, eye, brain, and lung tissues.

The second factor contributing to blurring is the random proton trajectories emitted from the MCS when they depart the object and travel towards the detector, a distance greater than zero from the object. This effect can be studied by merely elevating the PB momentum. The initial effect can be readily examined by raising the PB's intensity. It is evident from $\theta_0(z)$ and $y(z)$ that the results become progressively better in a linear fashion, as the momentum of the beam is increased. Multiplying the linear thickness of an object by the square root of the object thickness as a function of radiation length leads to even greater growth. Choosing a high momentum can effectively reduce blur to any desired degree for radiography of thick objects. For observing moving objects, the detectors need to be positioned at a distance from the object. The second effect is characterized by different methods of operation. The current approach to solving this issue hinges on the fact that protons possess a charge and their paths can be altered by a B-field, which can be achieved using an ML, as discussed in the following section. This

is in addition to PR processes, where a facile exponential equation is used for the angular scattering distribution and the nuclear attenuation based on a Gaussian MCS [12–13]. The proton transmission process in this approximation is $T(L) = \exp\left(-\sum_i \frac{L_i}{\lambda_i}\right)\left[1 - exp\left(-\frac{\theta_{cut}^2}{2\theta_0^2}\right)\right]$. A three-dimensional diagram of the variations of T (L) is shown in Fig. 4, illustrating its relationship with different z values and the incident proton energy of E for both water and various human tissues, including breast, eye, brain, and lung.

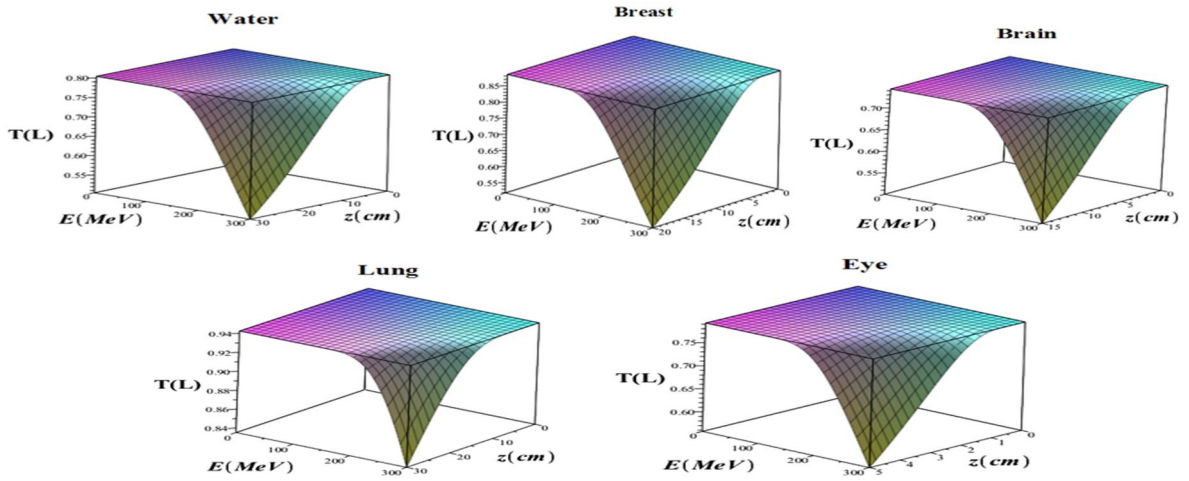

FIG. 4. 3-D diagram of $T(L)$ variations in terms of different values of z and incident proton kinetic energy of E in water and in breast, eye, brain, and lung tissues.

$\sum_i L_i$ is defined as the sum of L_i (the individual areal densities of each material), while λ_i is the factor of nuclear attenuation for i'th material: $\lambda_i = \frac{A_i}{N_A \sigma_i}$ .For the given expressions, the parameters can be defined as follows: N_A is equal to Avogadro's number; the absorption cross-section and atomic weight of the i'th material are shown by σ_i and A_i, respectively. θ_{cut} represents the angle-cut that includes the angular collimator. The X_{0i} (radiation length) parameter is defined as: $X_{0i} = \frac{716.4 A_i}{Z_i\,(Z_i+1)\ln(287/\sqrt{Z_i})}$. The initial component of T(L) pertains to attenuation, specifically nuclear attenuation, and is consistent with the X-ray attenuation process, whereas the second component is attributed to angular attenuation, a characteristic that distinguishes PR. Angular attenuation provides an alternative method for distinguishing material properties. The angular beam fraction broadening that forms the image for thick objects is determined by the material composition and the elastic scattering of proton-nucleon within the object itself [13]. The given equation should be accurate if the scattering angular distribution exhibits the same Gaussian momentum correlation spectrum. It is assumed that pixels a and b, which are crucial for observation in the lane of the image, are correlated with the quality of PR based on the contrast between them. The difference in transmission between these pixels is expressed as:

$$\Delta T = \exp\left(-\sum_i \frac{L_{ia}}{\lambda_i}\right)\left[1 - exp\left(-\frac{\theta_{cut}^2}{2\theta_{0a}^2}\right)\right] - \exp\left(-\sum_i \frac{L_{ib}}{\lambda_i}\right)\left[1 - exp\left(-\frac{\theta_{cut}^2}{2\theta_{0b}^2}\right)\right] \quad (2)$$

The cut-angle at its most favorable value can be found using Eq. (2). At high-energy, λ_i (the mean free path for the i'th material) parameter being roughly constant, the optimal cut-angle can be estimated by: $dT/d\theta_{cut} = 0$.

6.3. Magnetic Lens of PR System

The magnetic lens (ML) system, as illustrated in Fig.5, is designed in accordance with [14]. The two imaging lens cells have a magnification factor of negative one. Each cell contains four quadrupole magnets that operate under the same field strength, but they show alternating poles (+, –, +, –). The cell's configuration has a characteristic where protons are positioned radially around the midpoint between its two central magnets, based exclusively on their scattering angle in the object.

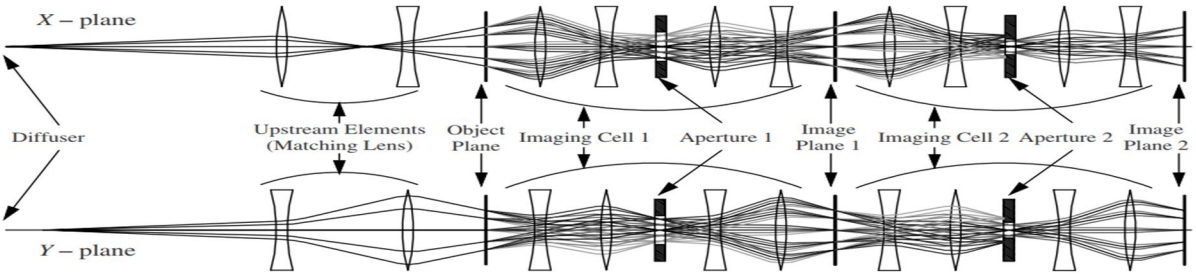

FIG. 5. Schematic illustration of the ML system, showing the X and Y planes.

Despite the fact that the appearance of the object's origin relates to a specific point in its plane, this topic enables the placement of a collimator in that specific location for making cuts on the MCS angle within the object. It was previously mentioned that the scattering distribution angle is in a Gaussian shape, with a width that can be calculated using the $\theta_0(z)$ relation. The collimator enables one to direct the particles at angles smaller than the cut angle (θ_{cut}), denoted by MCS. The number of transmitted particles N_C is given by: $N_C \approx N\left[1 - exp\left(-\frac{\theta_{cut}^2}{2\theta_0^2}\right)\right]$. In Error! Reference source not found., we plotted the 3D diagram of the $\frac{N_c}{N}$ variations in terms of different values of z and E in water and in breast, eye, brain, and lung tissues.

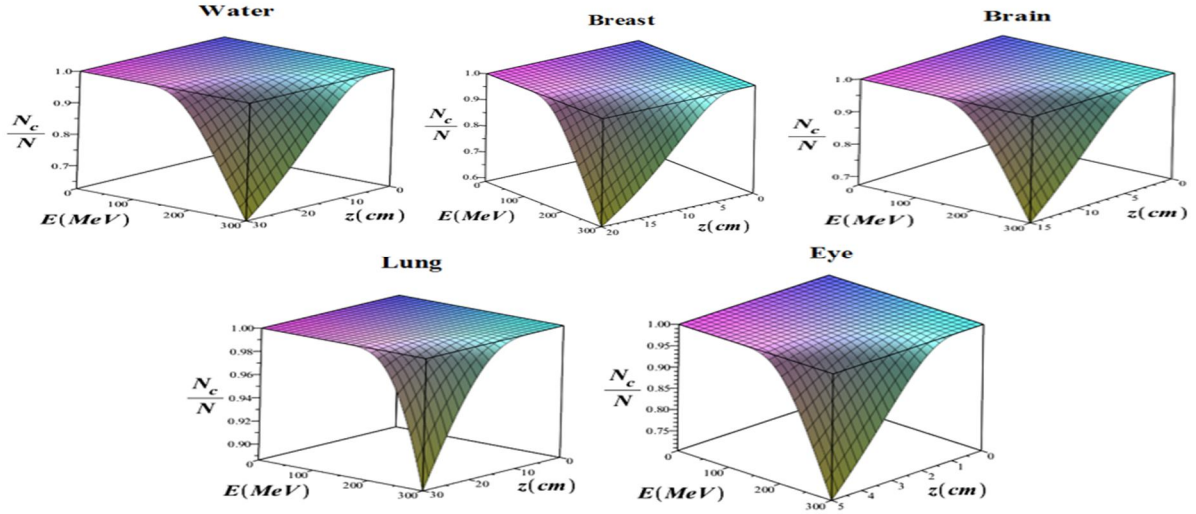

FIG. 6. 3-D diagram of $\frac{N_c}{N}$ variations in terms of different values of z and E in water and in breast, eye, brain, and lung tissues.

Here, the variable N represents the number of incident particles. When the value of θ_{cut} greatly exceeds θ_0 ,we anticipate that $N_c$will be equal to N. By substituting the $\theta_0(z)$ relation into the equation for θ_0 and simplifying, it can be found that $\frac{z}{X_0}$ is expressed as: $\frac{z}{X_0} \approx \frac{-\theta_c^2}{2\left(\frac{13.6MeV}{\beta cp}\right) ln\left(1-\frac{N_C}{N}\right)}$.

In Fig. 7, we depicted a three-dimensional diagram illustrating variations of $\frac{z}{X_0}$ with respect to z and E in water and in breast, eye, brain, and lung tissues.

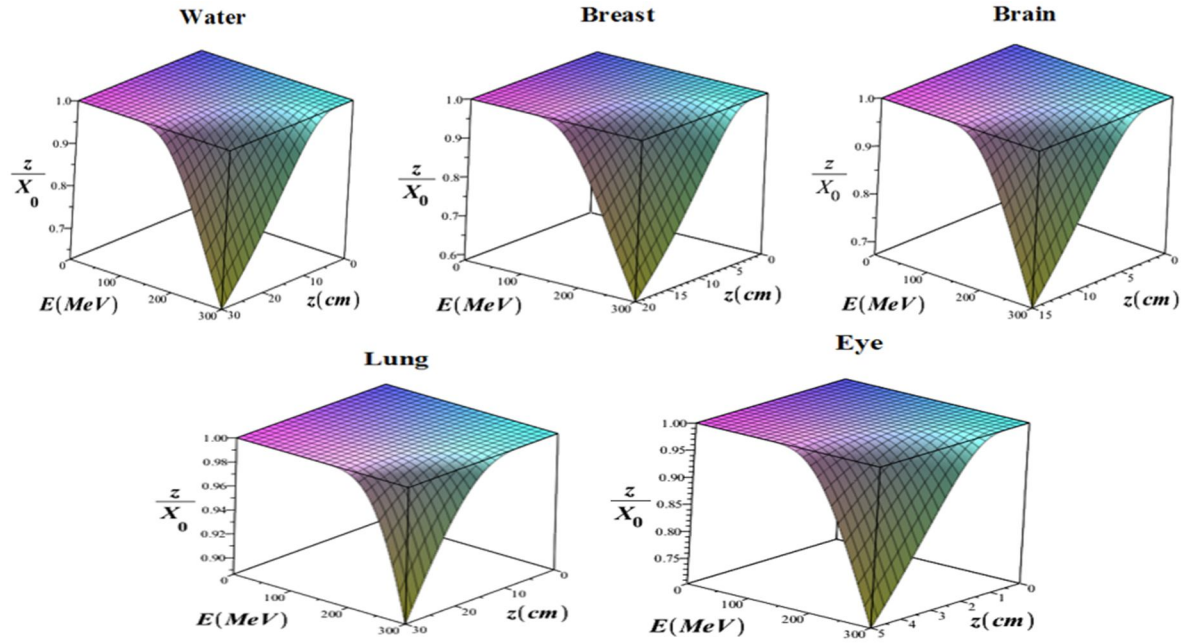

FIG. 7. 3D diagram of $\frac{z}{X_0}$ variations in terms of different values of z and E in water and in breast, eye, brain, and lung tissues.

When examining an ML system comprising two lenses (–I) mounted back-to-back, the first lens has an aperture that allows passage of all particles deflected by MCS, excluding those deflected by inelastic collisions. The second lens has its aperture set to cut into the MCS distribution. Detectors are then placed in the image plane of the two MLs and acquire two independent measurements. The first dependence is linked to the object's material in terms of nuclear interaction lengths, whereas the second dependence is related to the object's material in terms of radiation lengths. Because the values for nuclear interaction and radiation length have varying dependencies based on the type of material, we can thus determine both the quantity of existing material within the object and the type of material that exists in it. Using an ML with a single MCS cut angle can produce high-contrast PR, even when the object's thickness results in poor contrast through nuclear attenuation. For a thick object of a given thickness, an optimization cut-angle exists, which, as in the case of nuclear exponential beam attenuation, maximizes sensitivity to variations in object thickness when using pure MCS radiography. The optimal cut angle can be calculated using the same method that yielded equation λ=L/2, with the attenuation now expressed as $\frac{z}{X_0}$. The cut angle of MCS is generated by adjusting the aperture.

6.4. LET, Range, and Dose

The energy dissipation rate for a single proton with kinetic energy K that passes through the water is provided by $\left|\frac{dK}{d\lambda}\right|\left[MeV/(g/cm^2)\right] \approx \frac{1}{0.098k+0.0277}$. In medical applications, the relevant range for K is between 3 and 300 keV, which is expressed as κ = K / (100 [MeV]). The unit of λ is expressed as g.cm^{-2}, allowing consideration of its relationship with the thickness Δs (cm) of water, and $\Delta\lambda = \rho\Delta s$. The |dK/dλ| variations were graphed against the instantaneous kinetic energy K in the range 3 < K [MeV] < 300 for a single proton within the water, as shown in Fig. 8(a). The graph demonstrates a decrease in the average energy dissipation rate for the proton as K increases.

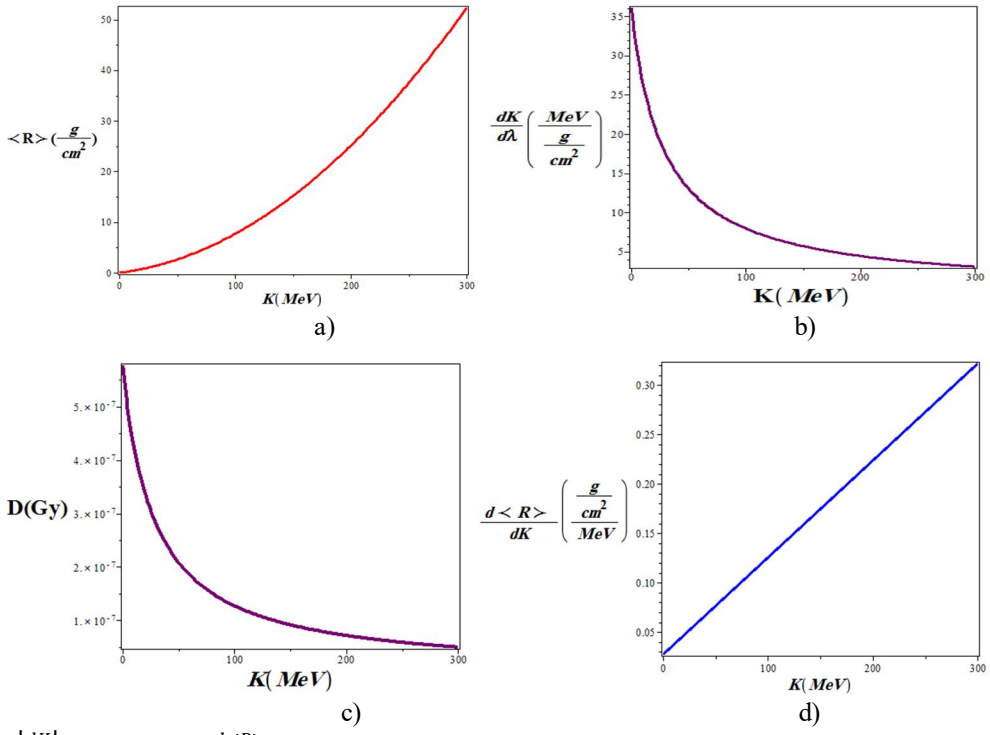

FIG. 8. a)$\left|\frac{dK}{d\lambda}\right|$, b) $< R >$, c) $\frac{d<R>}{dK}$, and d) average dose ($a = 0.1\ cm$) variations in terms of K in the interval $3 < K\ [MeV] < 300$ for a single proton in water.

The mean range ($R\ [gcm^{-2}]$) of a proton in water is: $< R > \approx 4.900\kappa^2 + 2.770\kappa$. Equations $\left|\frac{dK}{d\lambda}\right|$ and $< R >$ are not independent of each other. Hence, we have: $\frac{d<R>}{dK} = \left|\frac{dK}{d\lambda}\right|^{-1}$. In Fig. 8(b), the average range of proton variations versus K in water is plotted, with K being the variable of interest. The average number of protons in water exhibits a nonlinear increase with rising K levels, exhibiting the opposite trend compared to the average rate of energy dissipation caused by incident kinetic energy. In Error! Reference source not found.), the variations of $\frac{d<R>}{dK}$ in terms of the incident kinetic energy K of a single proton in water are shown, demonstrating a gradual nonlinear increase with increasing K. The instantaneous energy is maximized when K equals K_0, at which point λ is linked to the amplitude R. For example, a 200 MeV proton energy has a LET of about 4.47 $[MeV\ /\ (g\ /\ cm^2)]$ that exactly before it stops in the water at the end of its average range of about $226g\ /\ cm^2$, it increases significantly. Higher order approximations can be applied to Eq. (2) to improve the accuracy of low energy behavior, which is proportional to LET. The dose is expressed in grays, representing the total energy deposited per unit mass, measured in joules per kilogram. The average dose is obtained from the number of protons N passing through a square pixel of size a: $D \equiv \frac{N}{\rho a^2 \Delta s}\left|\frac{dK}{d\lambda}\right| \rho \Delta s = \frac{N}{a^2}\left|\frac{dK}{d\lambda}\right|$. Alternatively, it is simpler to write: $D[Gy] = 1.6 \times 10^{-10} \frac{N}{a^2[cm^2]}\left|\frac{dK}{d\lambda}\right| [MeV/({}^{g}/_{cm^2})]$. In Error! Reference source not found.), the average dose variations are plotted for the number of protons N passing through a square pixel of size a in terms of an incident kinetic energy of the proton, K. It is clear that the average dose declines as K increases. In Fig. 9, the 3D variations of the average dose are shown for N protons passing through a square pixel of size $a = 0.1\ cm$ in terms of the incident kinetic energy K in the range $3 < K\ [MeV] < 300$ and $10^5 < N < 10^6$. As seen in this figure, the average dose increases with increasing proton number, while it decreases with increasing proton beam energy, in good agreement with previous studies [40-41].

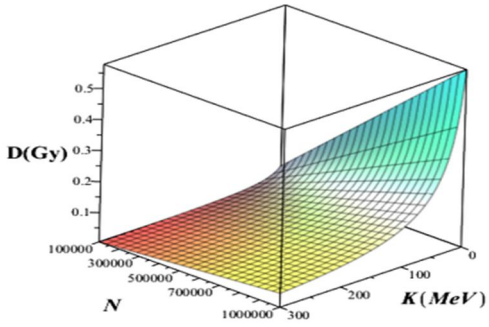

FIG. 9. 3D variations of the number of protons N passing through a square pixel with a size of 0.1 cm in terms of incident kinetic energy K in the range of $0 < K\,[MeV] < 300$ and $10^5 < N < 10^6$.

A proton with an energy of 200 MeV passing through a square pixel measuring 0.1 cm in size delivers an average dose of approximately 7.2×10^{-8}.

6.5. Adjustment

The loss of energy of protons in collisions with atomic electrons is governed by statistical principles. In addition to calculating the average, it is also necessary to verify the collection of dispersed RMS in energy dissipation and range [30-33]. A PB traversing a material with a thickness of Δλ can acquire the average square of the additional scattered energy: $\Delta\sigma_K^2 = 0.6\frac{Z}{A}(m_e c^2)^2\gamma\left(1-\frac{\beta^2}{2}\right)\Delta\lambda$. Here, m_e is the electron rest mass, Z and A are the atomic number and atomic weight of the element (pure) being traversed, and β and γ are the relativistic coefficients [15]. The three-dimensional diagram in Fig. 10 displays variations of $\Delta\sigma_K^2$ in relation to the kinetic energy of an incident proton (K) and the thickness (Δλ) for water and four distinct biological tissues: breast, brain, eye, and lung.

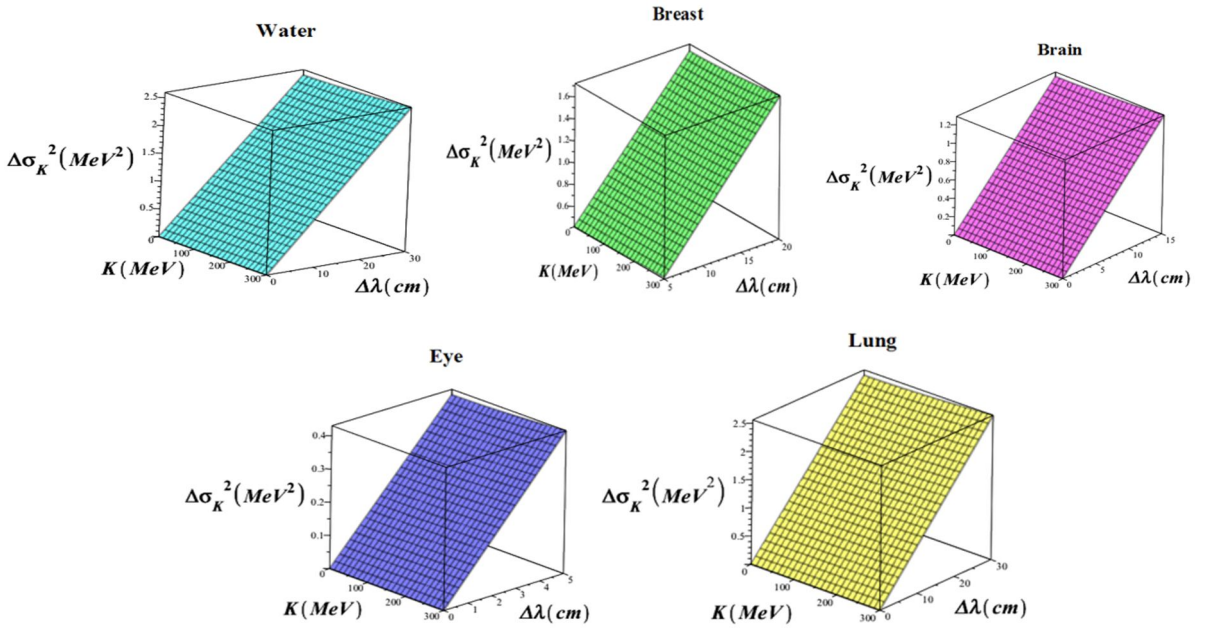

FIG. 1. 3D diagram of the variations of $\Delta\sigma_K^2$ in terms of the kinetic energy of an incident proton K and the thickness Δ for water and four different tissues: breast, brain, eye, and lung.

The growth rate is consistently uniform, and for water, it can be accurately approximated within the energy range relevant to medical applications as: $\sigma_K^2[MeV^2] \approx 0.089\lambda\left[{}^{g}/_{cm^2}\right]$. Immediately before stopping, the total RMS energy of a monochromatic proton beam can be expressed as: $\sigma_{KT}[MeV] = 0.30\sqrt{< R > [{}^{g}/_{cm^2}]}$. In Error! Reference source not found.(a), σ_{KT} variations are plotted as a function of the incident proton kinetic energy K in water. The figure clearly shows that σ_{KT} increases nonlinearly with increasing K.

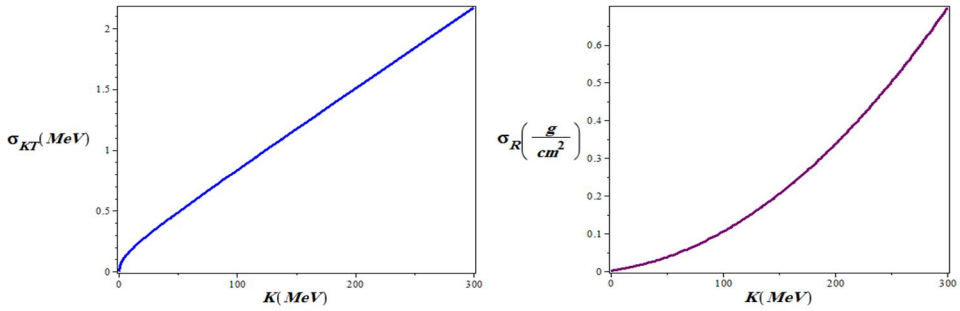

a) b)

FIG. 2. a) σ_{KT} and b) σ_R variations in terms of the kinetic energy of an incident proton K in water.

The phenomenon is linked to RMS range broadening: $\sigma_R = \frac{d<R>}{dK}\sigma_{KT}$, which can be approximated by: $\sigma_R\left[{}^{g}/_{cm^2}\right] \approx 0.300(0.0980\kappa + 0.0280)\,(4.900\kappa^2 + 2.770\kappa)^{1/2}$. For example, a monochromatic 200 MeV proton beam has an RMS kinetic energy spread of about 1.53 MeV at the end of its range of 26 g/cm^2, and an RMS range spread of about 0.34 g/cm^2 (0.34 cm in water). The spatial resolution of the radiographic image is defined by the RMS size of the beam on exit and, as a result, by the RMS range broadening if proton-by-proton track reconstruction is not possible or is not performed. In Error! Reference source not found.), we plotted σ_R variations in terms of the kinetic energy of an incident proton K in water. The data shown in this figure reveal an approximately nonlinear increase in the value of σ_R with rising K values in water (note that κ = K / (100 [MeV])). This is almost true for tissues, because, on average, approximately two-thirds of the human body is made up of water.

6.6. Mean Transmission Observation

The average transmission method, as depicted in Fig. 12 [16], is characterized by setting the incoming beam energy and bowtie filter properties such that the Bragg peak falls at the distal edge of the bowtie. This configuration optimizes the dose delivered to the patient while achieving maximum measurement sensitivity. The total linear density along a straight line is given by:

$$\lambda(x,y) = \int_A^B \rho(s)\,ds + \int_C^D \rho_{bowtie}\,ds \qquad (3)$$

$\lambda(x,y)$ is a function of the transverse coordinates x and y at the entrance. Bowtie filters are known to reduce the radiation dose at the periphery of the imaging field of view [1, 3], and they have also been shown to be effective in reducing scatter, a major source of image artifacts [1, 3, 4]. Additionally, they can help flatten the scatter distribution, which is beneficial for post-processing scatter correction strategies [7]. Typically, the thickness of a bowtie filter varies within the axial plane but remains constant along the third dimension, corresponding to the longitudinal field of view. Therefore, the material, thickness, and density of bowtie filters are important factors for image quality. From Eq. (3), $\lambda(x,y)$ depends on both the water density and the applied bowtie density. The value of $\lambda(x,y)$ influences the number of protons reaching the detector and, consequently, the resulting image quality. Simulation data indicate that the use of bowtie filters can reduce the ambient dose around the tissue. Furthermore, the bowtie filter design concepts are applied in this work to create a computational realization of a 3D human bowtie filter capable of achieving a constant effective attenuation coefficient across the entire field of view of human tissue.

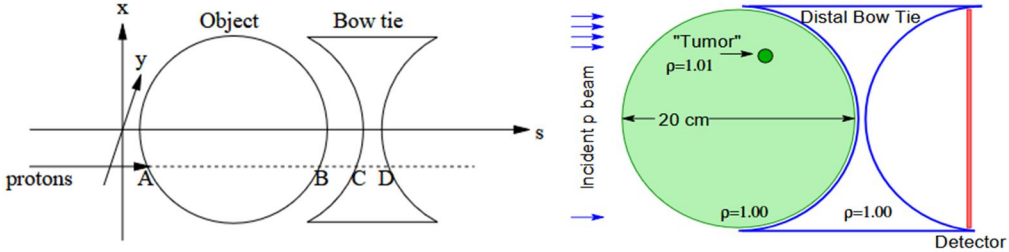

FIG. 3. Schematic design of the radiographed object with a "bowtie" compensator. The illustrated simple phantom can be used in initial reconstruction simulations [16].

The fraction of the transferred PB is a function of λ and an initial kinetic energy K_0, i.e., $T = T(\lambda, K_0)$. Transmission is measured for each square input pixel with a size of a: $T_{meas} = \frac{N_{out}}{N}$ .The number of input protons to each pixel is denoted as N, but only N_{out} is emitted from the bowtie and is subsequently transferred to a downstream detector. The accuracy of T_{meas} is indicated by the fact that T increases with the radiation proton number N: $T_{meas,\pm} = T \pm \frac{\sqrt{N_{out}}}{N} = T \pm \sqrt{\frac{T}{N}}$ .Note that in this relation, the quantity T is a function of λ and K_0. As a result, $T_{meas,\pm}$ becomes a function of K_0. In Figs. 13(a) and 13(b), we have plotted the 3D diagram of $T_{meas,+}$ and $T_{meas,-}$ variations for the $\pm$ signs in terms of T and N variations, respectively.

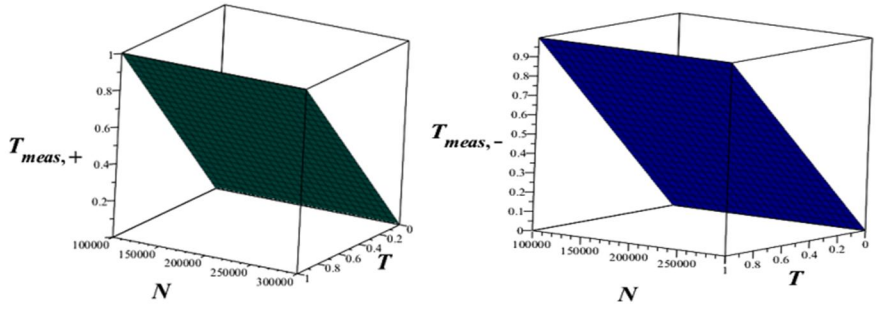

a) b)

FIG. 4. 3D diagram of a) $T_{meas,+}$ b) $T_{meas,-}$ variations in terms of changes of T and N.

The number of radiation protons required to alter the fractional change in density, expressed as $\delta \frac{\Delta\rho}{\rho_0}$, in a cubic voxel to a specific size 'a' needs to be determined. For the diagnosis of this kind of variation, the transmission T must be accurately quantified: $\Delta T = \frac{dT}{d\lambda}\Delta\lambda = \frac{dT}{d\lambda}\rho_0 a\delta$. $T_{meas,\pm}$ approximately shows that: $N \cong \frac{T}{\Delta T^2}$. Therefore, according to this relation, if the value of ΔT decreases, then the value of N increases, and as a result, according to $T_{meas,\pm} = T \pm \sqrt{\frac{T}{N}}$, the value of $T_{meas,\pm}$ increases.

Protons are necessary for each pixel's radiation. This outcome gives rise to a fundamental principle that yields a distinct radiography design: $N\delta^2 a^2 = \frac{T}{(\frac{dT}{d\lambda})^2 \rho_0^2}$. This expression can be applied straightforwardly to photons in X-ray imaging.

6.7. Sensitivity Response - Optimal Dose

Figure 14 implies that the right-hand side of the above relation can be minimized by adjusting the initial kinetic energy $K_0$to optimize the transfer gradient: $\frac{dT}{d\lambda}$, thereby maximizing sensitivity δ while minimizing dose D on the left-hand side. Studies in proton radiography indicate that the choice of analytical algorithms for more complex clinical imaging, such as lung or breast imaging, depends on the range distribution function. The range distribution φ(R) exhibits a substantial Landau tail. For practical purposes, a Gaussian approximation is reasonable: $\varphi(R) = \frac{1}{\sqrt{2\pi}\sigma_R}\exp\left(\frac{(R-<R>)^2}{2\sigma_R^2}\right)$. Note that the amount of beam spread is characterized by the quantity σ_R, which is an increasing function of the depth. Physically, this spread is due to the lateral scattering during the proton propagation. In addition, according to $< R > \approx 4.900\kappa^2 + 2.770\kappa$, this $\varphi(R)$ depends on the K.

Ignoring nuclear losses, we have: $\frac{dT}{d\lambda} = -\varphi(\lambda)$. and the maximum transfer gradient occurs when $\lambda =< R >$ and $T = 0.5$: $\left|\frac{dT}{d\lambda}\right|_{max} = \frac{1}{\sqrt{2\pi}\sigma_R}$. As a result, when the initial kinetic energy K_0 is altered so that half of the protons pass through into the object and the bowtie, we have: $N\delta^2 a^2 = \frac{\pi\sigma_R^2}{\rho_0^2}$. The local dose D that is delivered by this proton flux is a function of both the local energy of K and the initial energy K: $D\delta^2 a^4 = \frac{\pi\sigma_R^2}{\rho_0^2}\left|\frac{dK}{d\lambda}\right|$. When K equals$K_0$, at the patient's level, using equations $\frac{d<R>}{dK}$, σ_{KT}, and σ_R, we obtain: $D\delta^2 a^4 = \frac{0.089\pi}{\rho_0^2} < R > \frac{d<R>}{dK}$. Substituting $\left|\frac{dK}{d\lambda}\right|$ and σ_R yields the following suitable approximations:

$$N\delta^2 a^2[cm^2] \approx \frac{0.28}{\rho_0^2}(4.9k^2 + 2.8k)(0.10k + 0.03)^2 \quad (4)$$

and

$$Da^4\delta^2[Gy\ cm^4] \approx \frac{4.5\times10^{-11}}{\rho_0^2}(4.9k^2 + 2.8k)(0.10k + 0.03) \quad (5)$$

Here, $k \equiv {}^{K}/_{100}\,[MeV]$ and $\rho_0 \approx 1\,{}^{g}/_{cm^3}$. Note that, according to the above equations, both R and D are functions of $\varphi(R)$. In Error! Reference source not found., we plotted $N\delta^2 a^2$ and $D\delta^2 a^4$ variations in terms of the proton kinetic energy for water and for breast, brain, lung, and eye tissues. It is evident that as the kinetic energy of a proton rises, the values of $N\delta^2 a^2$ and $D\delta^2 a^4$ increase in a nonlinear fashion.

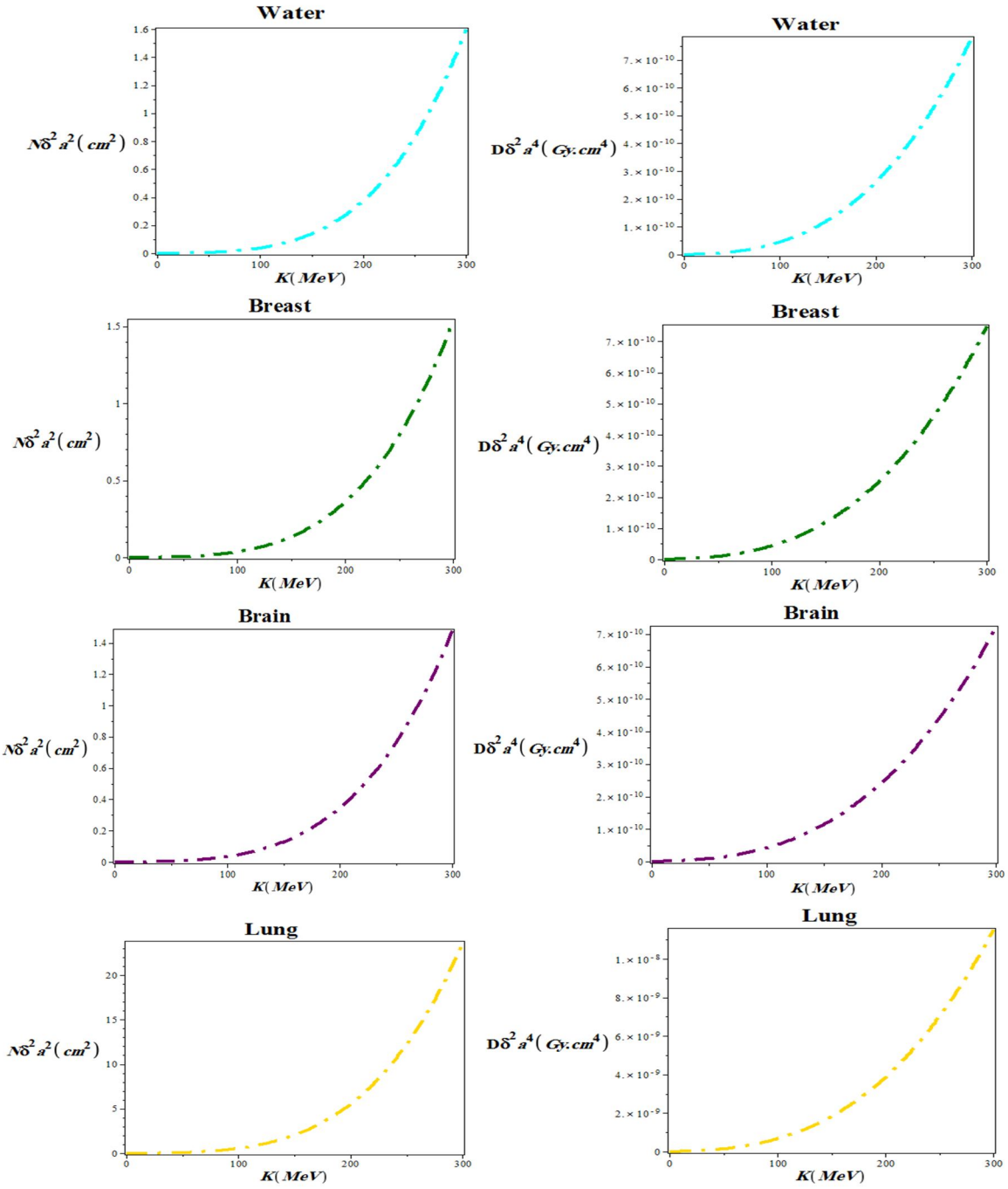

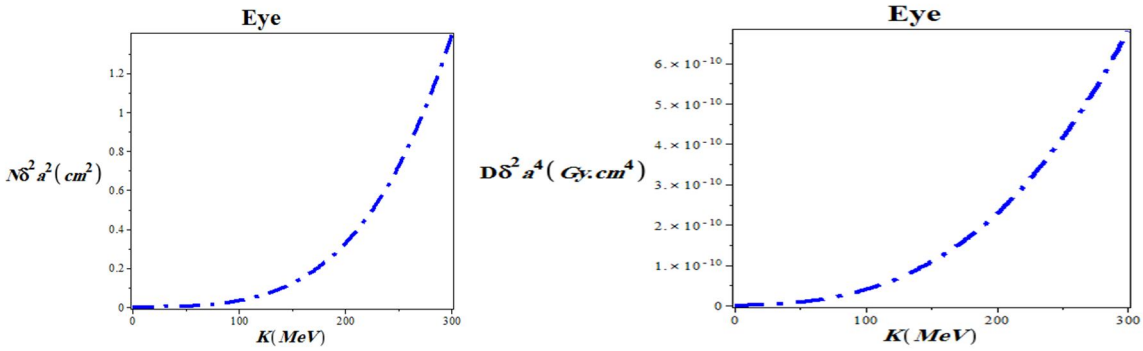

FIG. 5. $N\delta^2a^2$ and $D\delta^2a^4$ variations in terms of the kinetic energy of an incident proton in the range of $0 < K\,[MeV] < 300$ for water and breast, brain, lung, and eye tissues.

A PB with an energy of 200MeV is used in water for identifying density fluctuations, where the fluctuations, denoted as δ, are measured at a resolution of 0.01 in voxels with dimensions of a = 0.1 cm. In this case, N δ^2a^2 = 0.37, and the number of $N_0 = 3700000$ protons per pixel is required, resulting in a surface dose of $D = 26mGy$ for $K = 200\,MeV$. Eqs. (4) and (5) specify the dosage for a single radiographic image. In a computed tomography scan, for a field of view with a width of w, we have approximately: $M = \frac{W}{a}$. Accordingly, the total dose for CT scanning is scaled as: $D \sim \frac{W}{a^5\delta^2}$ .The relationship is heavily influenced by the voxel's size to the fifth power. In summary, results show that the nonlinear increase in Nδ^2a^2 and Dδ^2a^4 with increasing kinetic energy (K) are: transmission, $T(\lambda, K_0)$, the total linear density of a straight line, λ, initial kinetic energyK_0, number of input protons to each pixel, N, and σ_R parameter. Two factors are particularly important for proton radiography: (1) image resolution improves with accumulated proton shots (dose), but beyond a certain dose, further increases do not enhance resolution; (2) spatial resolution is higher for higher-energy protons due to their smaller scattering angle caused by MCS.

Studies indicate that CR39 detectors provide better resolution than RCF but are suitable only for low proton flux. Image blurring is mainly caused by MCS and represents out-of-focus blur. Applying non-blind image deblurring algorithms improves proton radiography image clarity and spatial resolution. With advances in petawatt (PW) lasers and target preparation technology, laser-driven proton energies are approaching 100 MeV and are expected to increase further. Therefore, a new generation of compact proton radiotherapy devices based on laser accelerators, along with associated proton radiography diagnostic systems, is highly probable. The methods presented here can also be extended to higher-energy protons.

6.8. Proton Energy Dissipation Through Proton

In transfer measurements, the energy of each individual proton is recorded rather than simply counting the fraction of exiting protons. This allows for an accurate reconstruction of energy dissipation within each voxel, which is critical for density mapping. It is assumed that a full-energy detector, such as a calorimeter, has a sensitivity limited by a minimum detectable dose. The reconstructed proton path is assumed to be sufficiently accurate to identify the specific voxel traversed by each proton. The total deposited energy for N protons passing through a square voxel of side a is equal to: $\Delta K = N\int\left|\frac{dK}{d\lambda}\right|\rho(s)ds \pm N^{1/2}\sigma_{KT}$. The second term indicates the measurement error in relation to the total fluctuation regulation, specifically: $\sigma_{KT} = \left(\int\frac{d\sigma_K^2}{d\lambda}\rho(s)ds\right)^{1/2}$ .A peculiar trait of PR is that proton trajectories are stochastic and not straight because protons undergo MCS. This is commonly accounted for by estimating the most likely path for each proton and performing line integrals along the resulting curvilinear lines. In addition to energy loss PR, other contrast mechanisms have been proposed, which exploit different types of interaction of protons with a medium. In particular, these are attenuation and scattering PR. The former measures the reduction in proton flux after an object due to inelastic nuclear interactions and reconstructs a map of the nuclear attenuation coefficient. The latter estimates the angular dispersion of protons due to MCS in the object and reconstructs a parameter describing MCS, e.g., radiation length. The error in measuring the average

energy dissipation per proton (ΔK / N) decreases statistically with a reduction of 1/√ N even for a full-calorimeter. Therefore, additional protons are required to resolve smaller density fluctuations in a single radiograph image. The average energy dissipation is provided by the formula, given that the density of a single voxel in this path varies at a rate of $\delta = \Delta\rho/\rho_0$:

$$\Delta\delta K = N\left|\frac{dK}{d\lambda}\right|\delta\rho_0 a \qquad (6)$$

The condition associated with this deviation from the density is diagnosed as: $\left|\frac{dK}{d\lambda}\right|\delta\rho_0 a > N^{1/2}\sigma_{KT}$. We placed the expressions of intensity and sensitivity on the left, and set the diagnosis threshold at: $N\delta^2 a^2 = \frac{1}{\rho_0^2}\frac{\sigma_{KT}^2}{|dK/d\lambda|^2}$. The relationship becomes dose-dependent, as indicated by $D = \frac{N}{a^2}\left|\frac{dK}{d\lambda}\right|$, and we have: $D\delta^2 a^4 = \frac{1}{\rho_0^2}\frac{\sigma_{KT}^2}{|dK/d\lambda|}$. One simpler method for our analysis is to first establish the amount: $N\delta^2 a^2[cm^2] \approx \frac{0.089\lambda}{\rho_0^2}(.10k + .03)^2$ and $D\delta^2 a^4[Gycm^4] \approx \frac{1.4\times10^{-11}\lambda}{\rho_0^2}(.10k + .03)$. Figure 15 illustrates three-dimensional representations of the variations in the number of protons (N) and local dose (D) in each radiography design, based on the kinetic energy of incident protons ranging from 0 to 300 MeV. A λ thickness of 0.01, with voxels of 0.1 cm in size, was drawn for water as well as breast, brain, lung, and eye tissues.

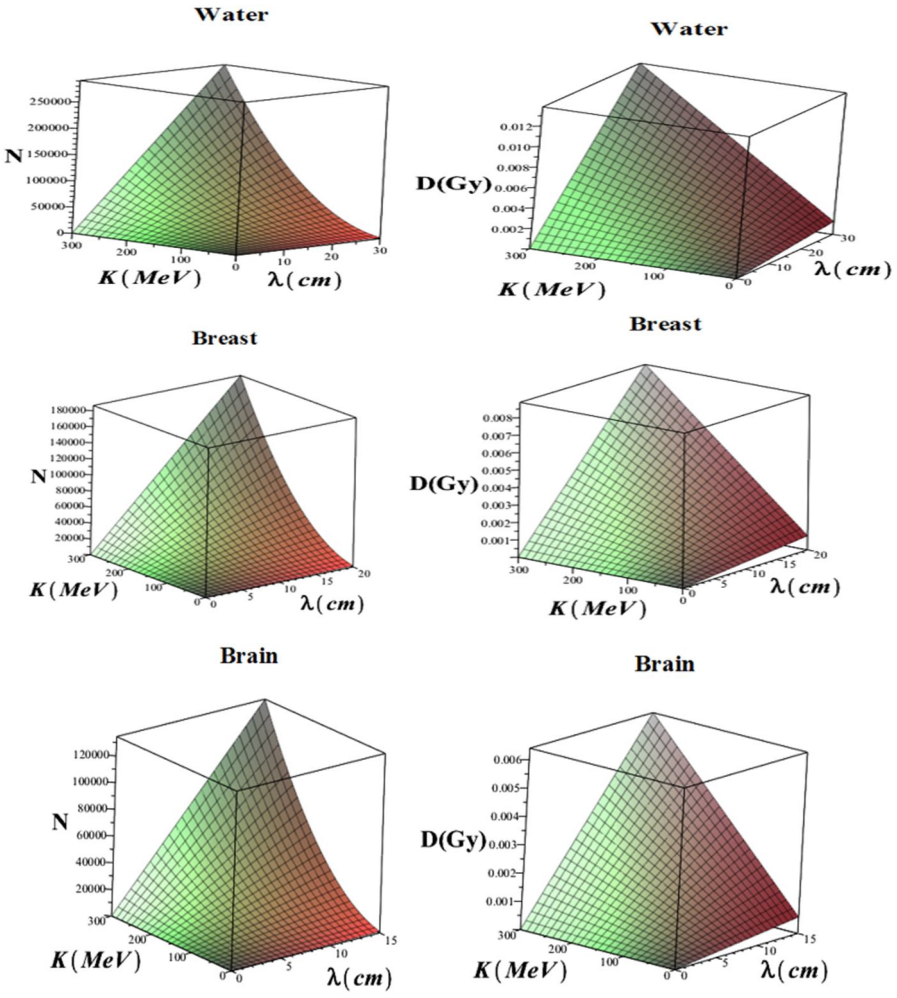

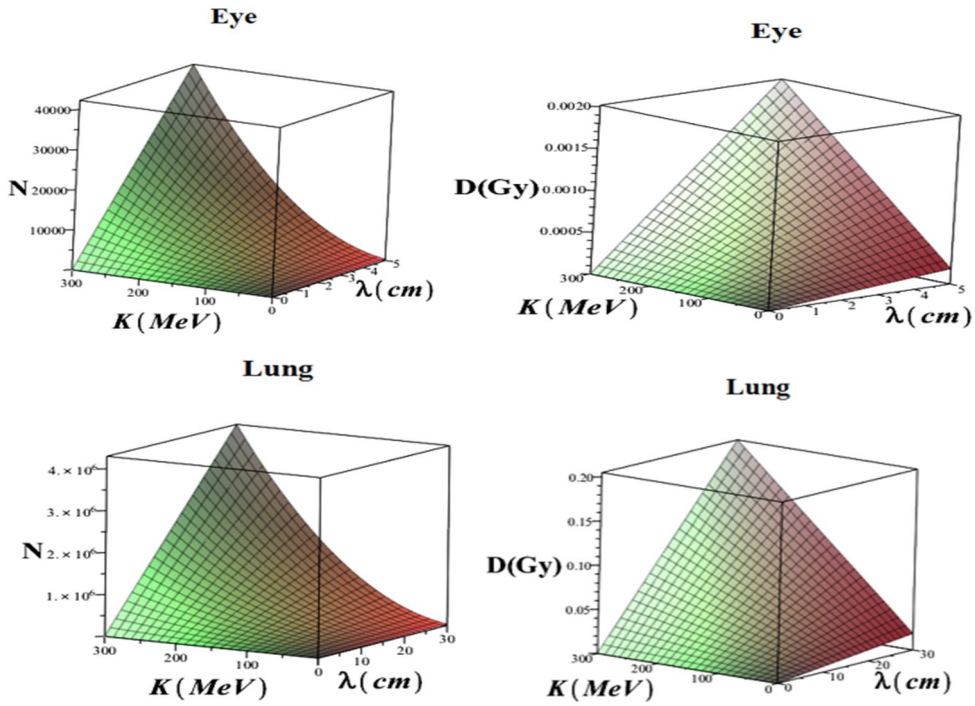

FIG. 6. 3D variations of N and D in terms of the kinetic energy of an incident proton in the range of $0 < K\,[MeV] < 300$ and thickness λ for $\delta = 0.01$ in voxels with the size of $a = 0.1\,cm$ in water and breast, brain, lung, and eye tissues.

λ is the patient's thickness. The instantaneous energy k is given by: $k \equiv {}^{K}/_{100}$,which is measured in MeV with a density of approximately $1.0\,{}^{g}/_{cm^3}$, denoted by ρ_0.The surface dose delivery is considered for a 200 MeV PB in water to detect density fluctuations of 0.01 in voxels with dimensions of 0.1 cm, for a thickness of $\lambda = 20\,g\,/\,cm^2$, since $Na\delta^2 \approx 0.094$ it is estimated that approximately 94000 protons are required to penetrate each pixel, and the local dose in each radiography project is approximately 6.6 mGy. At first glance, this dose is roughly half the size of the standard order, exceeding the amount normally received with the average transfer method.

Proton imaging is a promising technology for proton radiotherapy as it can be used for: (1) direct sampling of the tissue stopping power, (2) input information for multi-modality RSP reconstruction, (3) gold-standard calibration against concurrent techniques, (4) tracking motion, and (5) pre-treatment positioning. One of the limiting factors in imaging is noise. The imaging noise originates from two processes: the Coulomb scattering with the nucleus, producing a path deviation, and the energy loss straggling with electrons. Noise increases with the thickness of tissue traversed and decreases with higher proton energy. Scattering noise is dominant around high gradient edge whereas straggling noise is maximal in homogeneous regions. Image quality metrics are found to behave oppositely against energy, lower energy minimizes both the noise and the spatial resolution, with the optimal energy choice depending on the application and location in the imaged object.

7. Conclusions

In this work, simplified physical models of proton transport including Bethe-Bloch energy loss, energy straggling, and multiple Coulomb scattering (MCS) were employed in the 0–300 MeV energy range to analytically quantify the trade-offs and scaling relationships between dose, spatial resolution, density resolution, and voxel size. We found that the dose D is directly influenced by the voxel size alpha and the required density resolution δ, highlighting a strong dependence on voxel dimensions. Lens-focused proton radiography (PR) represents a novel imaging technique. Unlike X-ray radiography, PR employs a magnetic imaging lens system to achieve point-to-point focusing from the object to the scintillator screen, thereby minimizing blur caused by the angular divergence of scattered protons. The advantages of PR over conventional X-rays include precise

targeting of tumors, reduced radiation exposure to surrounding healthy tissues and organs, and diminished short-term and long-term side effects of radiation therapy. Clinically, PR also enables the detection of proton range variations due to anatomical changes in a patient, offering potential for improved treatment accuracy.

In general, it would be possible to use PR in combination with heavy ion gantries. The challenge in PR imaging arises from the MCS of the protons traversing different materials, causing blurring of the radiography image. Thus, to improve the image quality and identify each material in the phantom, cuts for the proton scattering angle have to be tuned carefully. The challenging matching conditions could be established already in front of the gantry and then mapped to the patient position (point-to-point focusing). Laser-driven ion accelerators can deliver high-energy, high-peak current beams and are thus attracting attention as a compact alternative to conventional accelerators. However, achieving sufficiently high energy levels suitable for applications such as PR remains a challenge for laser-driven ion accelerators.

References

[1] Engwall, E. et al., Med. Phys., 50 (9) (2023) 5723.

[2] Li, X. et al., Front. Oncol., 11 (2021) 698537.

[3] Mein, S. et al., Med. Phys., 49 (9) (2022) 6082.

[4] Klein, C. et al., Radiat. Oncol., 12 (2017).

[5] Rorvik, E., Fjera, L., Dahle, T., Dale, J., Engeseth, G., Stokkevag, C. et al., Phys. Med. Biol., 63 (2018).

[6] Gu, W., Ruan, D., Lyu, Q., Zou, W., Dong, L., Sheng, K., Med. Phys., 47 (2020) 2072.

[7] Zhang, G., Shen, H., Lin, Y., Chen, R., Long, Y., Gao, H., Med. Phys., 49 (2022) 5752.

[8] Wuyckens, S., Saint-Guillain, M., Janssens, G., Zhao, L., Li, X., Ding, X. et al., Comput. Biol. Med., 148 (2022).

[9] Engwall, E., Battinelli, C., Wase, V., Marthin, O., Glimelius, L., Bokrantz, R. et al., Phys. Med. Biol., (2022).

[10] Janson, M., Glimelius, L., Fredriksson, A., Traneus, E., Engwall, E., Med. Dosim., (2023).

[11] Tanabashi, M., Hagiwara, K., Hikasa, K., Nakamura, K., Sumino, Y., Takahashi, F., Agashe, K., Aielli, G., Amsler, C. et al., Phys. Rev. D, 98 (2018) 030001.

[12] Mein, S. et al., Radiother. Oncol., 199 (2024) 110434.

[13] Penfold, S. et al., J. Med. Radiat. Sci., 71 (2024) 27–36.

[14] Liu, G., Li, X., Zhao, L., Zheng, W., Qin, A. et al., Acta Oncol., (2020).

[15] Cao, W. et al., J. Appl. Clin. Med. Phys., 24 (2023) e13954.

[16] Paganetti, H., Botas, P., Sharp, G. et al., Phys. Med. Biol., 66 (2021) 22TR01.

[17] Giacometti, V., Hounsell, A., McGarry, C., Physica Medica, 76 (2020) 243–276.

[18] Thummerer, A., Zaffino, P., Meijers, A. et al., Phys. Med. Biol., 65 (2020) 095002.

[19] Thummerer, A., Seller Oria, C., Zaffino, P. et al., Med. Phys., 48 (2021) 7673–7684.

[20] O'Hara, C., Bird, D., Al-Qaisieh, B. et al., J. Appl. Clin. Med. Phys., 23 (2022) e13737.

[21] Seller Oria, C., Thummerer, A., Free, J. et al., Med. Phys., 48 (2021) 4498–4505.

[22] Thummerer, A., Seller Oria, C., Zaffino, P. et al., Med. Phys., 49 (2022) 6824–6839.

[23] Seller Oria, C., Thummerer, A., Free, J. et al., Med. Phys., 48 (2021) 4498–4505.

[24] Vanzi, E., Bruzzi, M., Bucciolini, M., Cirrone, G., Civinini, C., Cuttone, G. et al., Nucl. Instrum. Methods Phys. Res. A, 730 (2013) 184–190.

[25] Davies, J., Heuer, P., Bott, A., High Energy Density Phys., 49 (2023) 101067.

[26] Pearcy, J., Rosenberg, M., Johnson, T., Sutcliffe, G., Reichelt, B., Hare, J., Loureiro, N., Petrasso, R., Li, C., Phys. Rev. Lett., 132 (2024) 035101.

[27] Schaeffer, D., Fox, W., Follett, R., Fiksel, G., Li, C., Matteucci, J., Bhattacharjee, A., Germaschewski, K., Phys. Rev. Lett., 122 (2019) 245001.

[28] Li, C. et al., Phys. Rev. Lett., 123 (2019) 055002.

[29] Heuer, P., Leal, L., Davies, J. et al., Phys. Plasmas, 29 (2022) 072708.

[30] Tubman, E. et al., Nat. Commun., 12 (2021).

[31] Daido, H., Nishiuchi, M., Pirozhkov, A., Rep. Prog. Phys., 75 (2012) 056401.

[32] d'Humieres, E., Brantov, A., Bychenkov, V., Tikhonchuk, V., Phys. Plasmas., 20 (2013) 023103.

[33] Dover, N. et al., Phys. Rev. Lett., 124 (2020) 084802.

[34] Cristoforetti, G. et al., Sci. Rep., 7 (2017) 1479.

[35] Gizzi, L. et al., Appl. Sci., 7 (2017) 984.

[36] Gizzi, L. et al., Nucl. Instrum. Methods Phys. Res. A, 909 (2018) 160.

[37] Calestani, D., Villani, M., Cristoforetti, G., Brandi, F., Koester, P., Labate, L., Gizzi, L., Matter Radiat. Extremes, 6 (2021) 046903.

[38] Malko, S., Johnson, C., Schaeffer, D., Fox, W., Fiksel, G., Appl. Opt., 61 (2022) C133.

[39] Johnson, C., Malko, S., Fox, W., Schaeffer, D., Fiksel, G., Adrian, P., Sutcliffe, G., Birkel, A., Rev. Sci. Instrum., 93 (2022) 023502.

[40] Lysakovski, P., Besuglow, J., Kopp, B., Mein, S., Tessonnier, T., Ferrari, A. et al., Med. Phys., 50 (2023) 2510.

[41] Bashir, U., Siddique, M., Mclean, E., Goh, V., Cook, G., AJR, 207 (2016).